

Urban Air Temperature Prediction using Conditional Diffusion Models

Siyang Dai, Jun Liu, Ngai-Man Cheung
Singapore University of Technology and Design

Abstract

Urbanization as a global trend has led to many environmental challenges, including the urban heat island (UHI) effect. The increase in temperature has a significant impact on the well-being of urban residents. Air temperature (T_a) at 2m above the surface is a key indicator of the UHI effect. How land use land cover (LULC) affects T_a is a critical research question which requires high-resolution (HR) T_a data at neighborhood scale. However, weather stations providing T_a measurements are sparsely distributed e.g. more than 10km apart; and numerical models are impractically slow and computationally expensive. In this work, we propose a novel method to predict HR T_a at 100m ground separation distance (gsd) using land surface temperature (LST) and other LULC related features which can be easily obtained from satellite imagery. Our method leverages diffusion models for the first time to generate accurate and visually realistic HR T_a maps, which outperforms prior methods. We pave the way for meteorological research using computer vision techniques by providing a dataset of an extended spatial and temporal coverage, and a high spatial resolution as a benchmark for future research. Furthermore, we show that our model can be applied to urban planning by simulating the impact of different urban designs on T_a .

1. Introduction

Air temperature as a key climate variable is a critical factor in urban planning, energy consumption, and human well-being. To study the impact of urbanization, HR T_a data at neighborhood scale is essential. Weather stations can only provide highly sparse point measurements, which don't capture the fine-grained temperature patterns e.g. T_a around buildings or trees. Many studies on T_a [2, 25, 56] rely on the reanalysis dataset with super low spatial resolution. For example, ERA5 [19] has a gsd of 31km and the "land" variant [20] has 9km gsd. Our work is the first to provide a benchmark dataset for HR T_a prediction at 100m gsd. Researchers use numerical models to simulate HR T_a , but these models are computationally expensive due to the

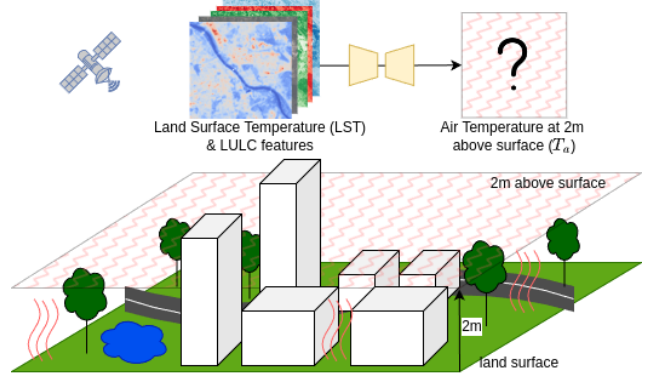


Figure 1. Task of HR T_a prediction given LST and LULC features derived from satellite imagery.

need of boundary conditions and forcing data etc. Take the Envi-Met software [22] as an example, a case study of microclimate's influence on vegetation with a small model (100x60x30 grids) takes about 164 hours with a Intel i7 CPU [23].

Prior works on T_a prediction lack a common benchmark. There is no common set of defined features, but frequently used are LST and LULC related features. The T_a resolution that can be predicted depends on the resolution of these input features. The authors of [12] try to estimate T_a at 5m gsd based on proprietary LiDAR data (used for deriving urban geometry) of very high density. However, the LiDAR and land use data as inputs does not align with the study period, during which the urban geometry may have changed significantly. Similar for other input features, it's very challenging or even impossible to obtain feature data that is both time-aligned and of HR (spatial and temporal). In this work, we create a benchmark dataset that not only contains the highest-resolution T_a that is publicly available, but we also ensure that all images in the dataset are time-aligned to the nearest hour. The details of the dataset will be discussed in Sec. 3.

We leverage diffusion models to predict T_a maps from various input features among which LST is the most important. We consider thermal conduction [9, 60], which is the spread of heat energy within a single material or across materials that are in contact with each other, as a diffusion pro-

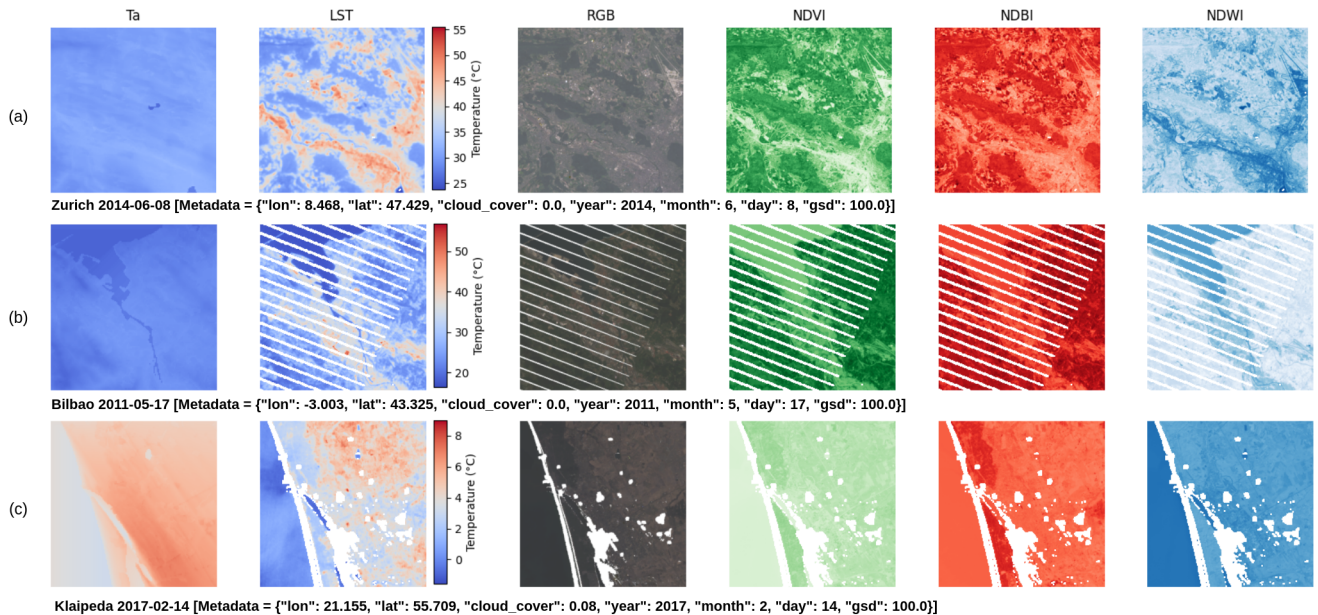


Figure 2. Illustration of LSTAT-20K dataset. Each row represents a paired-up sample of T_a , LST, RGB, NDVI, NDBI and NDWI images and metadata, with T_a and LST plotted on a common scale for visual comparison (T_a is generally more uniform and has a narrower range compared to LST). Samples (b) and (c) illustrate scan line failures and clouds on the satellite images respectively.

cess. Specifically, the temperature gradient along the vertical direction from land surface to 2m above the surface resembles the denoising diffusion process, where we regard the noise removed at each time step as the incremental temperature change over height. In addition, using diffusion models with conditional control can well preserve the spatial patterns in T_a maps.

In summary, our contributions are as follows: 1. We create a benchmark dataset for HR T_a prediction, which covers a wide spatial area with extended temporal span. 2. We propose a novel method to predict HR T_a leveraging diffusion models and achieve state-of-the-art performance. 3. We demonstrate the potential of our method in urban planning by simulating the impact of different urban designs on T_a .

2. Related work

2.1. Air temperature prediction

Most prior works on air temperature prediction are case studies of a single city or within a country for a limited time duration. The authors of [7] study the UHI characteristics of German cities using data from 2010 to 2012. Other similar works conduct studies respectively in Sydney from 2019 to 2022 [39], in Amsterdam for 4 months in 2017 [12], and in Hangzhou using 15 cloud free satellite images from 2006 to 2011 [47]. The majority of prior works focus on the thermal impact in summer times [57], leading to a lack of understanding of the seasonal temperature variations. Recently,

data-driven methods have been applied to prediction of urban air temperature. The prior studies use mostly statistical modelling [32, 47, 50, 63] and traditional machine learning models such as Random Forest [13–15, 21, 31, 54, 55], Multiple Linear Regression [4, 5, 8, 11, 16, 32], Gradient Boosting [12, 30], Support Vector Regression [27, 44], which don’t take advantage of the spatial patterns in the data. To our best knowledge, our work is the first to leverage diffusion models for HR T_a generation, which can yield high-fidelity and spatially coherent T_a maps.

2.2. Diffusion models

Diffusion models have achieved wide recognition in the computer vision community for their ability to generate high-quality images. Not only are diffusion models used for text-to-image applications [6, 10, 18, 41, 48], but they have also been applied to various inverse tasks such as image inpainting [38, 61, 68], super-resolution [58, 65], and deblurring [1]. Recently, studies on dense prediction [35, 40, 52] have also started to leverage diffusion models. Though diffusion models are stochastic in nature, methods [33, 37, 49] have been proposed to make them deterministic for dense prediction tasks. One milestone work in constraining generated images is the ControlNet [66], which takes guidance from conditioning images. Many works build on this idea to enable applications in different domains e.g. depth estimation [62], remote sensing [34], image editing [17], and super-resolution [36, 64]. We are the first to apply diffusion

models with ControlNet for HR T_a prediction.

3. Task and dataset

3.1. Task settings

We introduce three task settings for HR T_a prediction.

Same resolution. This is our baseline task that predicts T_a given LST and LULC features (RGB, NDVI, NDBI, and NDWI). Both target and input features are at the same resolution of 100m gsd, i.e. $LST^{100m} + LULC^{100m} \rightarrow T_a^{100m}$.

Super-resolution (SR). This setting applies when we have the more accessible low-resolution (LR) T_a available, such as LR simulation. We reduce the resolution of T_a by a factor of 3 and use it as an additional condition to predict the original resolution T_a , i.e. $T_a^{300m} + LST^{100m} + LULC^{100m} \rightarrow T_a^{100m}$.

Point SR. We further reduce the T_a to a few pixels, i.e. $T_a^{Npts} + LST^{100m} + LULC^{100m} \rightarrow T_a^{100m}$. This simulates the point measurements from weather stations, where N is the number of stations within the T_a map. We use a grid of 10km x 10km to sample the original T_a as the N point measurements.

On top of the two SR tasks, to push for highest resolution T_a prediction, we introduce the inferencing of T_a at 30m gsd given the 100m gsd T_a . As the ground truth for T_a^{30m} is not available, we directly inference using the models trained in the SR and Point SR settings, i.e. $T_a^{100m} + LST^{100m} + LULC^{30m} \rightarrow T_a^{30m}$. The evaluation is performed on a downsampled version of the generated T_a^{30m} images for comparison with original T_a^{100m} .

3.2. Dataset

We create a benchmark dataset to facilitate future research in HR T_a prediction. To achieve this, we source the target HR T_a from UrbClim¹ [29], and satellite imagery for LST and LULC features from Landsat [51].

UrbClim. An urban climate model that produces high-fidelity climate variables verified against in-situ measurements [3, 12, 24]. The T_a data provided supports UHI studies, but has not been previously combined with satellite imagery for a comprehensive CV benchmark. As mentioned in Sec. 1, climate simulation is expensive and slow, but data-driven methods based on such a benchmark can significantly improve the efficiency. Furthermore, with satellite imagery alone in the future, T_a can be predicted without the need for running new simulations. UrbClim covers a large spatial area of 100 European cities which exhibit a high variance in climate conditions, and an extended period from 2008 to 2017.

¹Generated using Copernicus Climate Change Service information, 2019. Neither the European Commission nor ECMWF is responsible for any use that may be made of the information or data it contains.

Landsat A series of Earth observation satellites that provide multi-spectral images at 30m spatial resolution and thermal infrared band at 100m effective resolution, and a temporal resolution of 16 days. We use Landsat’s multi-spectral bands to derive LST, NDVI, NDBI, NDWI, and RGB images for the dataset detailed in Sec. 3.2.1.

3.2.1. Data preparation and preprocessing

As first step to prepare the dataset, we use the cities in UrbClim to locate and download Landsat images. Then to pair up T_a and satellite data in location and time, we take the spatial coverage of each city as the mask to crop the satellite images, and use the timestamp of the satellite image to filter T_a up to hourly precision. Then we prepare the raw features from the multi-spectral bands. For LST, we directly scale the thermal infrared band (tir) using $lst = m * tir + a$, where m and a are the provided multiplier and bias. Then the indexes are computed using equations $ndvi = \frac{nir-red}{nir+red}$, $ndbi = \frac{swir-nir}{swir+nir}$, and $ndwi = \frac{nir-swir}{nir+swir}$, where nir, swir are the near-infrared, and short-wave infrared bands respectively. Note that T_a , LST, NDVI, NDBI, and NDWI are single-channel images. The 3-channel RGB images are created by stacking the red, green, and blue bands. Existing works [13, 16] take LULC as a key feature for the impact of different urban fabrics on T_a . LULC that aligns in time with T_a is rarely available, sometimes even years apart, which deteriorates the prediction accuracy. In our case, we innovatively use RGB images which inherently contain LULC information and are always synchronized with T_a . Likewise, the NDVI, NDBI, and NDWI indexes are used to capture impact of the vegetation, built-up areas, and water bodies on T_a respectively. We also prepare the metadata for each pair of T_a and input features including latitude, longitude, cloud cover, year, month, day and gsd. We show an illustration of the dataset in Fig. 2.

For image preprocessing, depending on the city size from UrbClim where $T_a \in \mathbb{R}^{101 \times 101} \sim \mathbb{R}^{401 \times 401}$, the satellite images are of $3.33 \times$ larger in size, ranging from $I_{sat} \in \mathbb{R}^{332 \times 332} \sim \mathbb{R}^{1334 \times 1334}$. To align with the input size of the pretrained model, we partition the larger ($> \mathbb{R}^{512 \times 512}$) satellite images into 512×512 patches and process the paired T_a images accordingly. Since LST has an effective resolution of 100m gsd, we downsample LST to the same size as T_a using bi-linear interpolation. This data preparation ensures no information loss during training.

One challenge in preparing Landsat satellite images is the invalid pixels due to the land-obstructing clouds and scan line failures with Landsat 7 [53]. Prior works [42, 46, 47] are inclined to select cloud-free images resulting in limited data. We, on the other hand, accept all images up to a 20% cloud cover and with scan line failures. We then inpaint the invalid pixels using the same diffusion framework as the one used for T_a prediction. Details are

provided in the supplementary material.

3.2.2. Dataset statistics and splits

Our dataset contains 100 cities in Europe, each with 10 years of data. The total geospatial area covered by the dataset is $59,179 \text{ km}^2$, averaging 591 km^2 per city. The preprocessing results in a total of 20,410 samples each containing images for T_a , LST, NDVI, NDBI, NDWI, and RGB along with the metadata. To this end, we name our dataset as *LSTAT-20K*. Temporal wise, the number of satellite images is limited by the Landsat revisit cycle and cloud cover requirement. Nonetheless, we try to include as many images to cover all months for each city, although certain cities and months have fewer samples due to more cloudy days. For example, continental cities have fewer samples than Mediterranean cities; and winter months have fewer samples than summer months. We show the distribution of the number of images per city and per month in the supplementary material.

We split the dataset into training and test sets using samples from years 2008 to 2015 and years 2016 to 2017 respectively, resulting a 3:1 ratio. The intuition is to train on the historical data and predict on future data to evaluate the generalization of the model.

4. Methodology

We are motivated by the idea that the gradual temperature change along the vertical direction from LST to T_a resembles the denoising diffusion process. By treating each incremental temperature change δT over a certain height δh to the noise removed at each sampling step, we consider the forward process to be adding noise to the target T_a image, and the reverse process to be removing the noise from the LST image. We first provide the background of diffusion models and ControlNet in Sec. 4.1. Then we describe our T_a prediction method DiffTemp in Sec. 4.2 and satellite images inpainting in the supplementary.

4.1. Background

Diffusion models. Diffusion models are a class of generative models by iteratively removing noise from a noise-perturbed image. DDPM [28] models the forward diffusion process by a Markov chain in Eq. (1) where $\bar{\alpha}_t$ is the variance schedule and $\epsilon_t \sim N(0, I)$ is the noise.

$$x_t = \sqrt{\bar{\alpha}_t}x_0 + \sqrt{1 - \bar{\alpha}_t}\epsilon_t, \quad t \in [1, T] \quad (1)$$

The schedule is designed to weight x_0 more at the beginning and ϵ more at the end, so the final x_T is close to pure Gaussian noise. Recovering the target data $x_0 \sim q(x_0)$ is by the reverse process in Eq. (2), where $p(x_{t-1}|x_t) \sim N(x_{t-1}; \mu_\theta(x_t, t), \Sigma_\theta(x_t, t))$. The diffusion network ϵ_θ that predicts the noise to be added at each step, is optimized with the objective $\mathbb{E}_{x_0 \sim q(x_0), \epsilon \sim N(0, I)} \|\epsilon - \epsilon_\theta(x_t, t)\|_2^2$. In

this work, we follow [66] to use the Stable Diffusion model [43], which performs the diffusion process in the latent space using the variational autoencoder (VAE).

$$p(x_{0:T}) = p(x_T) \prod_{t=1}^T p(x_{t-1}|x_t) \quad (2)$$

ControlNet. ControlNet [66] is a conditional diffusion model that controls the generation process with condition inputs such as depth or segmentation images. By reusing a trainable copy of the pre-trained layers of the original model and connecting back via zero-convolution layers, ControlNet can accurately drive Stable Diffusion to generate controlled images. We choose to leverage ControlNet for our task to preserve the spatial patterns in the input features.

4.2. Air temperature prediction

The model pipeline for HR T_a prediction is shown in Fig. 3. We use a combination of Stable Diffusion and ControlNet framework as in [66]. In summary, the main innovations include replacing the original noise schedule with a deterministic one to improve T_a prediction accuracy, and incorporating metadata into the conditional inputs to enhance guidance based on cues such as location and time. We provide the details in the following.

Noise scheduling. Typical text-to-image (T2I) generations are stochastic, so they use Eq. (1) to diffuse the target until Gaussian noise. We observe that by denoising from pure Gaussian noise, the generated temperature values are far from the target T_a . Motivated by the idea that thermal conduction process from LST to T_a resembles the denoising diffusion process, and inspired by scheduling ideas in [26, 35, 65], instead of diffusing and denoising the target image to and from pure noise, we use a scheduling strategy that takes advantage of the key feature LST. Specifically, we gradually add noise to the target T_a until close to LST in the forward diffusion process, then denoise from LST to the target T_a in the reverse process. The forward process now becomes Eq. (3), where x_0 is the T_a image and y is the LST image, both being used for all time steps. This way the model can learn the temperature patterns from the LST and predict the T_a values that are close to the target. Similar to the noise scheduling in Eq. (1), where x_t is more close to the target x_0 at the beginning and more close to pure noise ϵ towards the end, the new scheduling strategy in Eq. (3) weights the target x_0 (T_a) more at the beginning and y (LST) more towards the end, as $\bar{\alpha}_t$ decreases when the diffusion timestep t increases.

$$x_t = \sqrt{\bar{\alpha}_t}x_0 + \sqrt{1 - \bar{\alpha}_t}y, \quad t \in [1, T] \quad (3)$$

Metadata. Compared to natural images, bird-eye-view images like satellite and T_a images have their unique characteristics, such as the geographical location (latitude and

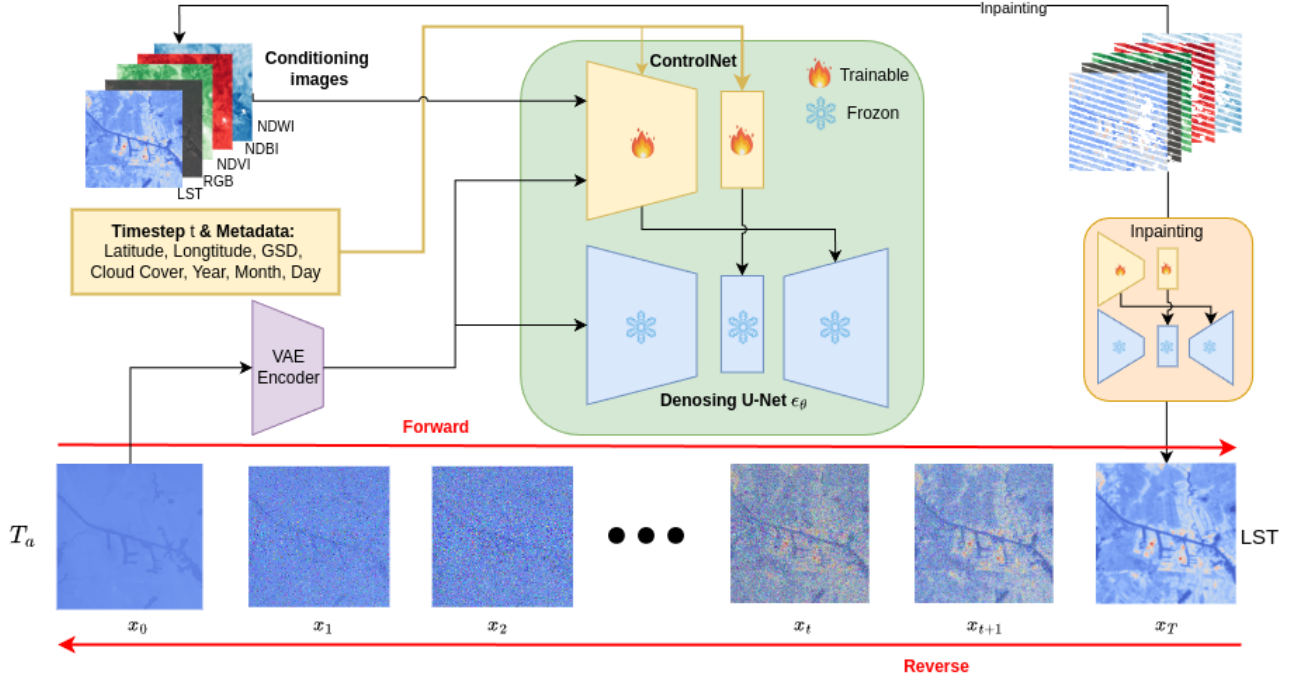


Figure 3. The pipeline of DiffTemp. The forward process adds noise to the target T_a image until close to the LST image. The ControlNet consumes the target latent of T_a and takes as conditioning images the satellite-derived LST, RGB and the index images and metadata. The denoising U-Net predicts the noise at each step given the target latent of T_a and residuals from ControlNet’s downsampling and middle blocks. The reverse process removes noise from the LST image to recover the target T_a image.

longitude) and the temporal information, which highly influence the temperature patterns and absolute values. We construct metadata of the conditioning images and feed them to the ControlNet to guide the generation process like in [34]. Specifically, the metadata embeddings are added to the time step t embedding as the input to the ControlNet. Apart from the influence of aforementioned time and location on T_a , as we split the dataset by different years for the training and test sets, we can assess the model’s generalization during inference since the model has never seen the test years’ data during training. The gsd helps the model to understand the spatial scale of the images, and cloud cover hints the model about the missing pixels in the satellite images.

We illustrate the pipeline of HR T_a prediction in Fig. 3. Specifically, the target image $x_0 \in \mathbb{R}^{H \times W \times 3}$ is encoded to the latent space $z_0 \in \mathbb{R}^{h \times w \times c}$ by the VAE encoder, where $(h, w) = (H/8, W/8)$ and c is the number of latent channels. The LST image y is encoded to z_y in the same way. The actual diffusion process is performed in the latent space by simply replacing x with z and y with z_y in Eq. (3). The latent z_t serves as input to both the ControlNet and the U-Net. The ControlNet also takes the concatenated LST and LULC images as conditions. The metadata and time step t embeddings are added then input to the downsampling and

middle blocks of the ControlNet. The residuals from ControlNet then guide the U-Net to predict at each step. Instead of predicting noise, we find using v-prediction [45] leads to better performance in our task. We use Eq. (4) as our objective to train the ControlNet, where $v = \sqrt{\bar{\alpha}_t}z_y - \sqrt{1 - \bar{\alpha}_t}z_t$ is the velocity term with z_y as the LST latent, and v_θ represents the U-Net and c is the residuals from ControlNet.

$$\mathcal{L}_{\text{mse}} = \mathbb{E}_{z_0, z_y} \|v - v_\theta(z_t, t, c)\|_2^2 \quad (4)$$

The reverse process is given in Eq. (5), where z_T is the LST latent encoded by the VAE encoder i.e. $z_T = \text{vae.enc}(LST)$, and the denoised \hat{z}_0 latent is expected to predict the desired $z_0 = \text{vae.enc}(T_a)$. The output \hat{z}_0 is decoded by the VAE decoder to obtain the final T_a image i.e. $T_a = \text{vae.dec}(\hat{z}_0)$. Note that the VAE decoder is omitted in the pipeline Fig. 3 for tidy look.

$$z_{t-1} = \sqrt{\bar{\alpha}_{t-1}}(\sqrt{\bar{\alpha}_t}z_t - \sqrt{1 - \bar{\alpha}_t}v_\theta(z_t, t, c)) + \sqrt{1 - \bar{\alpha}_{t-1}}z_y, \quad (5)$$

5. Experiments

We present the experimental analysis of our proposed method DiffTemp for HR T_a prediction on our dataset LSTAT-20K. We conduct extensive experiments to evaluate

and compare the performance of DiffTemp with prior methods. We also conduct an ablation study to analyze the impact of the noise scheduling strategy in the DiffTemp model.

5.1. Implementation details

Data resolution. (1) Same resolution task. As mentioned in Sec. 3.2.1, the LULC images have $3.33\times$ higher resolution (30m) than T_a and LST images (100m). To be specific, within a sample we have NDVI, NDBI, NDWI, and RGB images at a maximum of 512×512 resolution, and LST and T_a images at $0.3\times$ resolution of the satellite images, i.e. 154×154 at maximum. During training, we downsample the LULC images to the size of T_a and LST for alignment of the feature resolution. (2) SR and Point SR tasks. For the additional condition, we downsample T_a to $300m$ resolution, i.e. 52×52 at maximum, for the SR task. For the Point SR task, we sample N points from the T_a images as point measurements. We use the same sizes for the other images as in the same resolution task. Finally, all images are transformed to 512×512 before feeding into the model.

Training details. We employ the pretrained StableDiffusion [43] and the ControlNet architecture [66], and a U-Net that is pretrained on satellite images from [34]. We use the Adam optimizer with a learning rate of $5e-5$ and a batch size of 4, and update the model weights for 300k training steps. More specifically, we fine-tune for each of the 100 cities in the dataset for 3k steps.

Compared methods. We set `n_estimators=100`, `max_depth=10` for both Random Forest and Gradient Boosting, and `alpha=0.1` for Linear Regression, and `hidden_layer_sizes=(64,128,64)`, `lr=0.001` for MLP.

Evaluation metrics. We evaluate the performance of the T_a prediction model using mean absolute error (MAE) and root mean squared error (RMSE) in degree celcius following the common practice in prior works [7, 39, 57, 67]. In addition, we involve a new metric Structural Similarity Index (SSIM) [59] to evaluate the spatial patterns preserved in the predicted T_a maps.

5.2. Experimental results

We show the results for the three task settings in this section. As there is no public benchmark dataset for HR T_a prediction, we compare our method with the frequently used methods in prior works by the same-resolution task setting. We select 4 representative methods for comparison: Random Forest (RF), Gradient Boosting Decision Tree (GBDT), Linear Regression (LR), and Multi-layer Perceptron (MLP), of which RF and GBDT are the best performing methods in most prior works. In order to make a fair comparison, we utilize the same data features for all methods. Specifically, we use LST, NDVI, NDBI, NDWI, and RGB as well as the metadata as input features and T_a as target for all methods. Since the machine learning (ML) models

Method	RMSE↓	MAE↓	SSIM↑
Random Forest	3.72	3.45	0.32
Gradient Boosting	3.44	3.25	0.36
Linear Regression	2.84	2.63	0.23
MLP	3.54	3.42	0.45
DiffTemp (ours)	2.20	2.09	0.70

Table 1. Comparison of the prior methods with DiffTemp on LSTAT-20K.

Task	RMSE↓	MAE↓	SSIM↑
Super-resolution (SR)	0.920	0.849	0.779
T_a^{30m} with SR	1.950	1.704	0.710
Point SR	1.707	1.588	0.724
T_a^{30m} with Point SR	2.469	2.197	0.664
Same resolution	2.208	2.097	0.701

Table 2. Evaluation of the SR and Point SR tasks and the inference on T_a^{30m} with the respective model trained.

require tabular data, we build a dataset that regards a pixel as a data entry. We train a separate model for each city in the dataset for better capturing the city-specific patterns. To rule out the effect of the inpainted pixels, we use the raw data for training and evaluate only on the valid pixels.

Same resolution. We show in Tab. 1 the performance of all the methods on LSTAT-20K dataset. It can be seen that our method DiffTemp outperforms the prior methods by a large margin, especially in terms of SSIM. This indicates that DiffTemp can better capture the spatial patterns in the T_a maps, in addition to the low physical errors by metrics MAE and RMSE. It’s worth noting that even though the Linear Regression model has lower MAE and RMSE than the RF and GB models, it has the lowest SSIM score, which exposes the limitation of regression methods to only mimic the target distribution of temperature values without understanding the spatial patterns.

To further illustrate the effectiveness of DiffTemp, we show in Fig. 4 the visual comparison of the predicted T_a maps by DiffTemp and the prior methods. It can be seen that the ML methods tend to follow the input LST features, which actually ranks the highest in the feature importance analysis of Random Forest model. For example, in Sample (a), RF and Linear Regression models predict the T_a maps that are very similar to the LST maps, and same for RF model in Sample (d). In Sample (c), the ML methods deviate a lot from the ground truth. This indicates that ML models are not able to generalize well to all the samples.

SR and Point SR. By using the same model architecture as in Sec. 4.2 with the downsampled T_a as an additional conditioning image, we train and evaluate the model on the

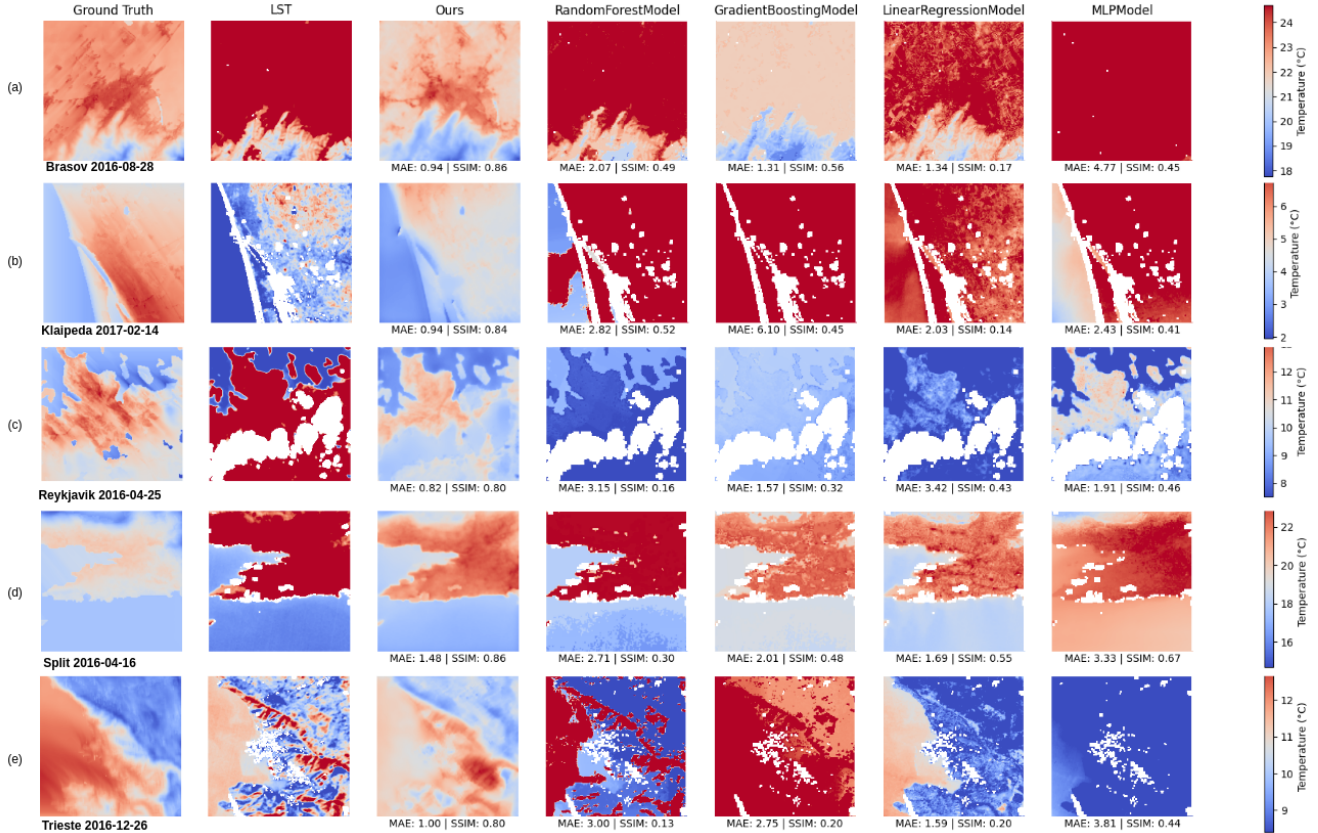


Figure 4. Qualitative comparison of the predicted T_a maps by ours (DiffTemp) and the prior methods.

two task settings, and inference T_a^{30m} with the same model trained. We show the experimental results in Tab. 2.

As the results show, when incorporating either the down-sampled T_a or the point measurements as an additional condition, the model performance improves compared to the baseline task. The SR task achieves better performance than the Point SR task. This is expected since the downsampled T_a contains more spatial information than the point measurements.

The inference on T_a^{30m} with the model trained on SR task performs better than Point SR. This indicates the model better transfers SR knowledge trained from $300m \rightarrow 100m$ to the inference task $100m \rightarrow 30m$ than Point SR. However, even with point measurements alone, we can derive a meaningful T_a map with reasonable accuracy and perceptual quality. This enables future application incorporating weather station measurements.

5.3. Ablation study

We investigate the impact of the noise scheduling strategy in the DiffTemp model, and show the results in Tab. 3. The results show a large performance gap between the pure noise scheduling and the LST noise scheduling. This is expected

Method	RMSE↓	MAE↓	SSIM↑
Pure noise scheduling	6.09	6.26	0.44
LST noise scheduling	2.20	2.09	0.70

Table 3. Ablation of the two types of noise scheduling.

as pure noise scheduling is for stochastic generation of images, where diversity weighs more than fidelity. Though it fails to enforce a physical constraint on the generated T_a images, the perceptual performance measured by SSIM is still better than the ML methods.

6. Potential applications

Urban planning use case. To illustrate the potential of DiffTemp in urban planning, we simulate different urban designs by inserting different land features (denoted by $mask_{new}$) in the RGB images. Due to the change of land features, the LST images should also change accordingly. We build a model based on the same diffusion architecture to predict LST images from the RGB images alone. Specifically, we use RGB as the condition and LST as the target image. We use the noise scheduling strategy in Eq. (1). At

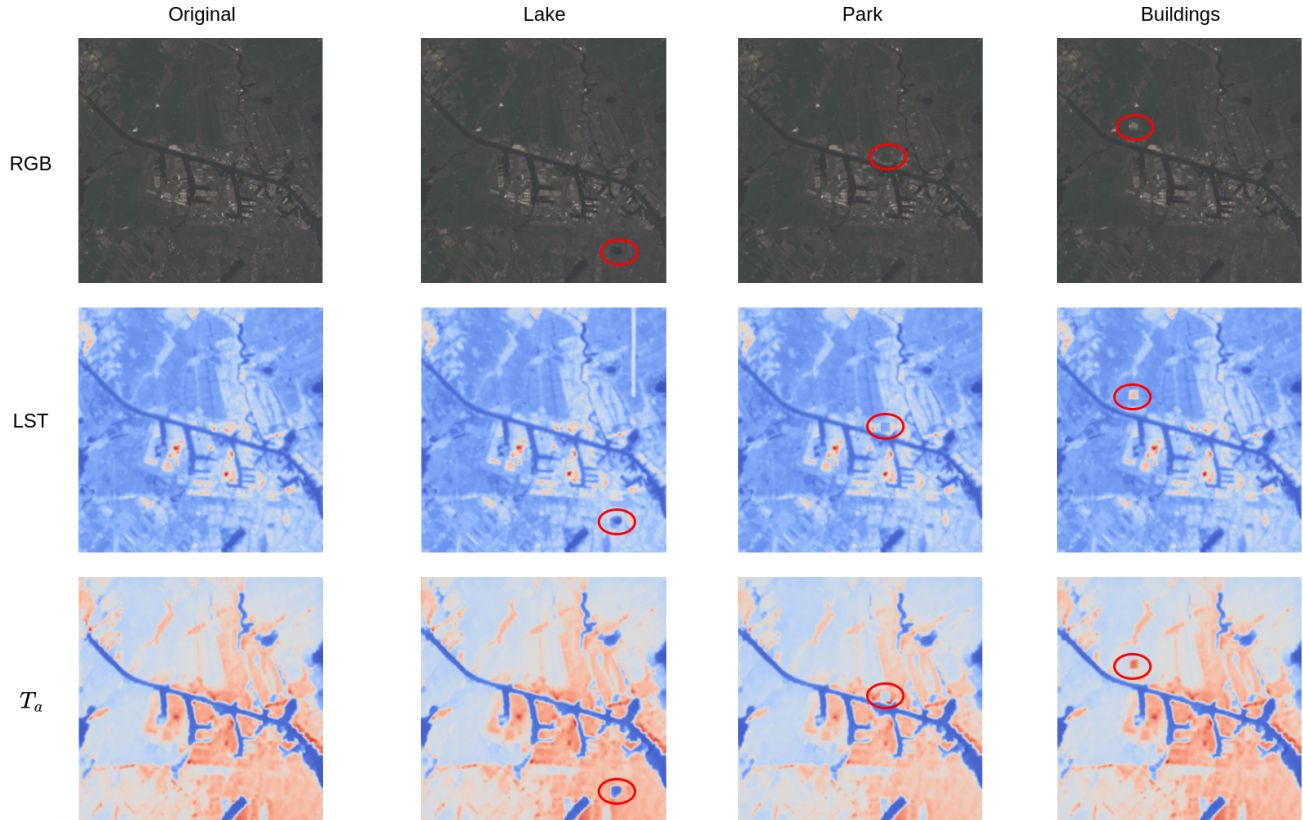


Figure 5. By simulating different urban designs, we show the impact of water bodies, green spaces, and buildings on the air temperature at neighborhood scale. Note: LST and T_a are not drawn to the same scale for better visualizing the temperature characteristics within the image.

inference, given a modified RGB image with new land features, we generate new LST from the diffusion model. With new RGB and LST inputs, we take them as the conditions and predict new T_a using the trained DiffTemp model.

In particular, we simulate 3 types of urban designs: 1. insert water bodies (e.g. lake) in a vegetated area; 2. insert green spaces (e.g. park) in the residential area; 3. insert buildings (e.g. industry park) in the undeveloped area where vegetation is dominant. Each newly inserted land feature is about 20×20 pixels which is equivalent to $600m \times 600m$ in the real world. We illustrate the results in Fig. 5. It can be observed that the T_a maps are significantly influenced by the new land features: water bodies and green spaces tend to lower the T_a while buildings tend to increase the T_a . With this use case, we demonstrate the potential of DiffTemp in helping urban planners to assess the microclimate impact of different urban designs.

Other applications With the SR and Point SR task settings, we enable prediction of HR T_a maps from LR data sources and point observations respectively, which is more practical in real-world scenarios. With the predicted HR T_a , we further empower the study of UHI effect, energy de-

mand, and human well-being.

7. Conclusion

We propose a new benchmark for high-resolution (HR) air temperature (T_a) prediction, which is critical for urban planning, energy consumption, and human well-being. Our dataset, LSTAT-20K, is the first to provide HR T_a data with a large spatial area and extended temporal coverage. We also are the first to leverage conditional diffusion models for this task which has not been well studied from the CV perspective. The extensive experiments demonstrate the effectiveness of our method in predicting T_a not only for the physical accuracy but also for the perceptual quality. We further present a use case of our method in urban planning, which highlights an alternative approach other than costly numerical simulations for urban microclimate studies.

References

- [1] Refusion: Enabling Large-Size Realistic Image Restoration with Latent-Space Diffusion Models | IEEE Conference Publication | IEEE Xplore. <https://ieeexplore.ieee.org/document/10208651>. 2
- [2] Spatial Downscaling of ERA5 Reanalysis Air Temperature Data Based on Stacking Ensemble Learning. <https://www.mdpi.com/2071-1050/16/5/1934>. 1
- [3] Urbclim a fast urban boundary layer climate model. <https://explore.openaire.eu/search/publication?pid=10.1016%2Fj.uclim.2015.01.001>. 3
- [4] Lucille Alonso and Florent Renard. Integrating Satellite-Derived Data as Spatial Predictors in Multiple Regression Models to Enhance the Knowledge of Air Temperature Patterns. *Urban Science*, 3(4):101, 2019. 2
- [5] Lucille Alonso and Florent Renard. A New Approach for Understanding Urban Microclimate by Integrating Complementary Predictors at Different Scales in Regression and Machine Learning Models. *Remote Sensing*, 12(15):2434, 2020. 2
- [6] Omri Avrahami, Dani Lischinski, and Ohad Fried. Blended Diffusion for Text-driven Editing of Natural Images. In *2022 IEEE/CVF Conference on Computer Vision and Pattern Recognition (CVPR)*, pages 18187–18197, 2022. 2
- [7] Benjamin Bechtel, Klemen Zakšek, Jürgen Oßenbrügge, Gedrius Kaveckis, and Jürgen Böhner. Towards a satellite based monitoring of urban air temperatures. *Sustainable Cities and Society*, 34:22–31, 2017. 2, 6
- [8] Benjamin Bechtel, Klemen Zakšek, Jürgen Oßenbrügge, Gedrius Kaveckis, and Jürgen Böhner. Towards a satellite based monitoring of urban air temperatures. *Sustainable Cities and Society*, 34:22–31, 2017. 2
- [9] Vanesa Bobes-Jesus, Pablo Pascual-Muñoz, Daniel Castro-Fresno, and Jorge Rodriguez-Hernandez. Asphalt solar collectors: A literature review. *Applied Energy*, 102:962–970, 2013. 1
- [10] Tim Brooks, Aleksander Holynski, and Alexei A. Efros. Instructpix2pix: Learning to follow image editing instructions. In *2023 IEEE/CVF Conference on Computer Vision and Pattern Recognition (CVPR)*, pages 18392–18402, 2023. 2
- [11] Jie Cao, Weiqi Zhou, Zhong Zheng, Tian Ren, and Weimin Wang. Within-city spatial and temporal heterogeneity of air temperature and its relationship with land surface temperature. *Landscape and Urban Planning*, 206:103979, 2021. 2
- [12] Fatemeh Chajaei and Hossein Bagheri. Machine learning framework for high-resolution air temperature downscaling using LiDAR-derived urban morphological features. *Urban Climate*, 57:102102, 2024. 1, 2, 3
- [13] Guangzhao Chen, Yuan Shi, Ran Wang, Chao Ren, Edward Ng, Xiaoyi Fang, and Zhihua Ren. Integrating weather observations and local-climate-zone-based landscape patterns for regional hourly air temperature mapping using machine learning. *Science of The Total Environment*, 841:156737, 2022. 2, 3
- [14] Shisheng Chen, Wen Zhang, Nyuk Hien Wong, and Marcel Ignatius. Combining CityGML files and data-driven models for microclimate simulations in a tropical city. *Building and Environment*, 185:107314, 2020.
- [15] Shihan Chen, Yuanjian Yang, Fei Deng, Yanhao Zhang, Duanyang Liu, Chao Liu, and Zhiqiu Gao. A high-resolution monitoring approach of canopy urban heat island using a random forest model and multi-platform observations. *Atmospheric Measurement Techniques*, 15(3):735–756, 2022. 2
- [16] Xuan Chen, Jiachuan Yang, Chao Ren, Sujong Jeong, and Yuan Shi. Standardizing thermal contrast among local climate zones at a continental scale: Implications for cool neighborhoods. *Building and Environment*, 197:107878, 2021. 2, 3
- [17] Xi Chen, Lianghua Huang, Yu Liu, Yujun Shen, Deli Zhao, and Hengshuang Zhao. AnyDoor: Zero-shot Object-level Image Customization. In *Proceedings of the IEEE/CVF Conference on Computer Vision and Pattern Recognition*, pages 6593–6602, 2024. 2
- [18] Shin-I Cheng, Yu-Jie Chen, Wei-Chen Chiu, Hung-Yu Tseng, and Hsin-Ying Lee. Adaptively-realistic image generation from stroke and sketch with diffusion model. In *2023 IEEE/CVF Winter Conference on Applications of Computer Vision (WACV)*, pages 4043–4051, 2023. 2
- [19] Copernicus Climate Change Service (C3S). Era5: Fifth generation of ecmwf atmospheric reanalyses of the global climate, 2024. [Online; accessed 28-October-2024]. 1
- [20] Copernicus Climate Change Service (C3S). Era5-land: Land component of the fifth generation of ecmwf atmospheric reanalyses of the global climate, 2024. [Online; accessed 28-October-2024]. 1
- [21] Ahmed H. M. Eldesoky, Nicola Colaninno, and Eugenio Morello. High-resolution air temperature mapping in a data-scarce, arid area by means of low-cost mobile measurements and machine learning. *Journal of Physics: Conference Series*, 2042(1):012045, 2021. 2
- [22] ENVI-met. Envi-met official website, 2024. [Online; accessed 28-October-2024]. 1
- [23] ENVI-met. Vegetation in envi-met, 2024. [Online; accessed 28-October-2024]. 1
- [24] Markel García-Díez, Dirk Lauwaet, Hans Hooyberghs, Joan Ballester, Koen De Ridder, and Xavier Rodó. Advantages of using a fast urban boundary layer model as compared to a full mesoscale model to simulate the urban heat island of Barcelona. *Geoscientific Model Development*, 9(12):4439–4450, 2016. 3
- [25] Qian He, Ming Wang, Kai Liu, Kaiwen Li, and Ziyu Jiang. GPRChinaTemp1km: A high-resolution monthly air temperature data set for China (1951–2020) based on machine learning. *Earth System Science Data*, 14(7):3273–3292, 2022. 1
- [26] Eric Heitz, Laurent Belcour, and Thomas Chambon. Iterative α \$(-de)Blending: A Minimalist Deterministic Diffusion Model, 2023. 4
- [27] Hung Chak Ho, Anders Knudby, Paul Sirovyak, Yongming Xu, Matus Hodul, and Sarah B. Henderson. Mapping max-

- imum urban air temperature on hot summer days. *Remote Sensing of Environment*, 154:38–45, 2014. 2
- [28] Jonathan Ho, Ajay Jain, and Pieter Abbeel. Denoising diffusion probabilistic models. In *Advances in Neural Information Processing Systems*, pages 6840–6851. Curran Associates, Inc., 2020. 4
- [29] H. Hooyberghs, J. Berckmans, D. Lauwaet, F. Lefebvre, and K. De Ridder. Climate variables for cities in europe from 2008 to 2017, 2019. DOI: 10.24381/cds.c6459d3a (Accessed on 04-Apr-2024). 3
- [30] Ian Hough, Allan C. Just, Bin Zhou, Michael Dorman, Johanna Lepeule, and Itai Kloog. A multi-resolution air temperature model for France from MODIS and Landsat thermal data. *Environmental Research*, 183:109244, 2020. 2
- [31] Christopher Hutengs and Michael Vohland. Downscaling land surface temperatures at regional scales with random forest regression. *Remote Sensing of Environment*, 178:127–141, 2016. 2
- [32] Nasime Janatian, Morteza Sadeghi, Seyed Hossein Sanaeinejad, Elham Bakhshian, Ali Farid, Seyed Majid Hashemini, and Sadegh Ghazanfari. A statistical framework for estimating air temperature using MODIS land surface temperature data. *International Journal of Climatology*, 37(3):1181–1194, 2017. 2
- [33] Tero Karras, Miika Aittala, Timo Aila, and Samuli Laine. Elucidating the design space of diffusion-based generative models. In *Proc. NeurIPS*, 2022. 2
- [34] Samar Khanna, Patrick Liu, Linqi Zhou, Chenlin Meng, Robin Rombach, Marshall Burke, David Lobell, and Stefano Ermon. DiffusionSat: A Generative Foundation Model for Satellite Imagery, 2024. 2, 5, 6
- [35] Hsin-Ying Lee, Hung-Yu Tseng, Hsin-Ying Lee, and Ming-Hsuan Yang. Exploiting Diffusion Prior for Generalizable Dense Prediction, 2024. 2, 4
- [36] Xinqi Lin, Jingwen He, Ziyan Chen, Zhaoyang Lyu, Bo Dai, Fanghua Yu, Wanli Ouyang, Yu Qiao, and Chao Dong. Diff-BIR: Towards Blind Image Restoration with Generative Diffusion Prior, 2024. 2
- [37] Cheng Lu, Yuhao Zhou, Fan Bao, Jianfei Chen, Chongxuan Li, and Jun Zhu. Dpm-solver: A fast ode solver for diffusion probabilistic model sampling in around 10 steps. *arXiv preprint arXiv:2206.00927*, 2022. 2
- [38] Andreas Lugmayr, Martin Danelljan, Andres Romero, Fisher Yu, Radu Timofte, and Luc Van Gool. RePaint: Inpainting using Denoising Diffusion Probabilistic Models, 2022. 2
- [39] Marzie Naserikia, Melissa A. Hart, Negin Nazarian, Benjamin Bechtel, Mathew Lipson, and Kerry A. Nice. Land surface and air temperature dynamics: The role of urban form and seasonality. *Science of The Total Environment*, 905: 167306, 2023. 2, 6
- [40] Quang Nguyen, Truong Vu, Anh Tran, and Khoi Nguyen. Dataset diffusion: Diffusion-based synthetic data generation for pixel-level semantic segmentation. *Advances in Neural Information Processing Systems*, 36, 2024. 2
- [41] Tanzila Rahman, Hsin-Ying Lee, Jian Ren, Sergey Tulyakov, Shweta Mahajan, and Leonid Sigal. Make-a-story: Visual memory conditioned consistent story generation. In *2023 IEEE/CVF Conference on Computer Vision and Pattern Recognition (CVPR)*, pages 2493–2502, 2023. 2
- [42] Priyanka Rao, Patrizia Tassinari, and Daniele Torreggiani. Exploring the land-use urban heat island nexus under climate change conditions using machine learning approach: A spatio-temporal analysis of remotely sensed data. *Heliyon*, 9(8):e18423, 2023. 3
- [43] Robin Rombach, Andreas Blattmann, Dominik Lorenz, Patrick Esser, and Björn Ommer. High-resolution image synthesis with latent diffusion models. In *Proceedings of the IEEE/CVF Conference on Computer Vision and Pattern Recognition (CVPR)*, pages 10684–10695, 2022. 4, 6
- [44] S. Salcedo-Sanz, R. C. Deo, L. Carro-Calvo, and B. Saavedra-Moreno. Monthly prediction of air temperature in Australia and New Zealand with machine learning algorithms. *Theoretical and Applied Climatology*, 125(1):13–25, 2016. 2
- [45] Tim Salimans and Jonathan Ho. Progressive Distillation for Fast Sampling of Diffusion Models, 2022. 5
- [46] S. Sameh, F. Zarzoura, and M. El-Mewafi. Automated Mapping of Urban Heat Island to Predict Land Surface Temperature and Land use/cover Change Using Machine Learning Algorithms: Mansoura City. *International Journal of Geoinformatics*, 18(6):47–67, 2022. 3
- [47] Li Sheng, Xiaolu Tang, Heyuan You, Qing Gu, and Hao Hu. Comparison of the urban heat island intensity quantified by using air temperature and Landsat land surface temperature in Hangzhou, China. *Ecological Indicators*, 72:738–746, 2017. 2, 3
- [48] Yujun Shi, Chuhui Xue, Jun Hao Liew, Jiachun Pan, Hanshu Yan, Wenqing Zhang, Vincent Y. F. Tan, and Song Bai. DragDiffusion: Harnessing Diffusion Models for Interactive Point-based Image Editing, 2024. 2
- [49] Jiaming Song, Chenlin Meng, and Stefano Ermon. Denoising diffusion implicit models. *arXiv:2010.02502*, 2020. 2
- [50] Annette Straub, Katja Berger, Susanne Breitter, Josef Cyrus, Uta Geruschkat, Jucundus Jacobeit, Benjamin Kühnbach, Thomas Kusch, Andreas Philipp, Alexandra Schneider, Robin Umminger, Kathrin Wolf, and Christoph Beck. Statistical modelling of spatial patterns of the urban heat island intensity in the urban environment of Augsburg, Germany. *Urban Climate*, 29:100491, 2019. 2
- [51] U.S. Geological Survey. Landsat-7/8/9 image data. <https://www.usgs.gov/landsat-missions>. Accessed: 15-Oct-2024. 3
- [52] Junjiao Tian, Lavisha Aggarwal, Andrea Colaco, Zsolt Kira, and Mar Gonzalez-Franco. Diffuse attend and segment: Unsupervised zero-shot segmentation using stable diffusion. In *Proceedings of the IEEE/CVF Conference on Computer Vision and Pattern Recognition*, pages 3554–3563, 2024. 2
- [53] U.S. Geological Survey. What is landsat 7 etm+ slc-off data?, 2023. Accessed: 04-Nov-2024. 3
- [54] Zander S. Venter, Oscar Brousse, Igor Esau, and Fred Meier. Hyperlocal mapping of urban air temperature using remote sensing and crowdsourced weather data. *Remote Sensing of Environment*, 242:111791, 2020. 2
- [55] Zander S. Venter, Tirthankar Chakraborty, and Xuhui Lee. Crowdsourced air temperatures contrast satellite measures of

- the urban heat island and its mechanisms. *Science Advances*, 7(22):eabb9569, 2021. [2](#)
- [56] Mosisa Tujuba Wakjira, Nadav Peleg, Paolo Burlando, and Peter Molnar. Gridded daily 2-m air temperature dataset for Ethiopia derived by debiasing and downscaling ERA5-Land for the period 1981–2010. *Data in Brief*, 46:108844, 2023. [1](#)
- [57] Han Wang, Jiachuan Yang, Guangzhao Chen, Chao Ren, and Jize Zhang. Machine learning applications on air temperature prediction in the urban canopy layer: A critical review of 2011–2022. *Urban Climate*, 49:101499, 2023. [2](#), [6](#)
- [58] Yufei Wang, Wenhan Yang, Xinyuan Chen, Yaohui Wang, Lanqing Guo, Lap-Pui Chau, Ziwei Liu, Yu Qiao, Alex C. Kot, and Bihan Wen. SinSR: Diffusion-Based Image Super-Resolution in a Single Step, 2023. [2](#)
- [59] Zhou Wang, A.C. Bovik, H.R. Sheikh, and E.P. Simoncelli. Image quality assessment: from error visibility to structural similarity. *IEEE Transactions on Image Processing*, 13(4): 600–612, 2004. [6](#)
- [60] Wikipedia contributors. Thermal conduction, 2024. Accessed: 2024-11-04. [1](#)
- [61] Shaoan Xie, Zhifei Zhang, Zhe Lin, Tobias Hinz, and Kun Zhang. Smartbrush: Text and shape guided object inpainting with diffusion model. In *Proceedings of the IEEE/CVF Conference on Computer Vision and Pattern Recognition*, pages 22428–22437, 2023. [2](#)
- [62] Lihe Yang, Bingyi Kang, Zilong Huang, Xiaogang Xu, Jiashi Feng, and Hengshuang Zhao. Depth Anything: Unleashing the Power of Large-Scale Unlabeled Data. In *Proceedings of the IEEE/CVF Conference on Computer Vision and Pattern Recognition*, pages 10371–10381, 2024. [2](#)
- [63] Chaeyeon Yi, Yire Shin, and Joon-Woo Roh. Development of an Urban High-Resolution Air Temperature Forecast System for Local Weather Information Services Based on Statistical Downscaling. *Atmosphere*, 9(5):164, 2018. [2](#)
- [64] Fanghua Yu, Jinjin Gu, Zheyuan Li, Jinfan Hu, Xiangtao Kong, Xintao Wang, Jingwen He, Yu Qiao, and Chao Dong. Scaling Up to Excellence: Practicing Model Scaling for Photo-Realistic Image Restoration In the Wild. In *Proceedings of the IEEE/CVF Conference on Computer Vision and Pattern Recognition*, pages 25669–25680, 2024. [2](#)
- [65] Zongsheng Yue, Jianyi Wang, and Chen Change Loy. ResShift: Efficient Diffusion Model for Image Super-resolution by Residual Shifting. [2](#), [4](#)
- [66] Lvmin Zhang, Anyi Rao, and Maneesh Agrawala. Adding conditional control to text-to-image diffusion models. In *2023 IEEE/CVF International Conference on Computer Vision (ICCV)*, pages 3813–3824, 2023. [2](#), [4](#), [6](#)
- [67] Wenbin Zhu, Aifeng Lǚ, and Shaofeng Jia. Estimation of daily maximum and minimum air temperature using MODIS land surface temperature products. *Remote Sensing of Environment*, 130:62–73, 2013. [6](#)
- [68] Yuanzhi Zhu, Kai Zhang, Jingyun Liang, Jiezhang Cao, Bihan Wen, Radu Timofte, and Luc Van Gool. Denoising Diffusion Models for Plug-and-Play Image Restoration, 2023. [2](#)